JOURNAL OF AIRCRAFT
Vol. 47, No. 2, March–April 2010

Airborne Lidar for Automatic Feedforward Control of Turbulent In-Flight Phenomena

Guillermo Jenaro Rabadan*
Airbus France, 31060 Toulouse, France
and
Nikolaus P. Schmitt,† Thomas Pistner,‡ and Wolfgang Rehm§
EADS Innovation Works, 81663 Muenchen, Germany

DOI: 10.2514/1.44950

Design, development, installation, and flight test of a novel airborne forward-looking lidar sensor are presented, aiming at accurately and remotely measuring the airspeed in front of the aircraft for automatic control of turbulence in-flight phenomena. The development is driven by the stringent requirements of the capability of measuring airspeed at cruise altitude, in clear air, and at all weather environments with the required precision. The sensor was installed in an A340-300 testbed for flight testing, inside a dedicated fairing in a forward-looking configuration. The flight-test measurements proved that the direct-detection Rayleigh/Mie lidar is capable of detecting the wind speed under flight-test conditions up to 39,000 ft in clear air, rain, dense clouds, and ice rain. A measurement range of 50 m is achieved for the ultraviolet lidar at a 60 Hz update rate and at a standard deviation of line-of-sight speed as low as 1.0–1.5 m/s. Those parameters, as required for forward-looking automatic control sensors, are a unique basis for the usage of such a remote sensor for automatic turbulence control.

Nomenclature

h	=	gap between the etalon plates, mm
$I(\lambda, \theta)$	=	fringe intensity, W/m^2
k_B	=	Boltzmann constant 1.38×10^{-23} kg · m^2/s^2 · K
m	=	molecular mass, for example, air about $28.96 \times 1.66 \times 10^{-27}$, kg
R	=	reflection coefficient of etalon
T	=	outside air temperature, K
T_r	=	transmission coefficient of etalon
U^e	=	matrix, for which the columns contain the components of the unitary vectors aligned with each of the LOS directions in a given reference frame, m/s
$\boldsymbol{V}_{A/C}$	=	aircraft translational speed, m/s
V_{compLOS}	=	aircraft's motion-induced speed to be compensated, m/s
$V_{w\text{LOS}}$	=	turbulence wind speed projected onto the line of sight, m/s
V_{LOS}	=	line-of-sight measured speed, m/s
$\{V^e\}$	=	three components of the airspeed given in the same reference axes, m/s
$\{V^e_{\text{ap}}\}$	=	best approximation for the wind in the least-squares sense, m/s
v	=	relative speed, m/s
z	=	altitude, km
$\beta(\lambda)$	=	wavelength-dependent Rayleigh backscatter coefficient, cm^{-1} sr^{-1}
Δf	=	Doppler frequency shift, Hz
λ	=	laser wavelength, nm
$\Delta \boldsymbol{V}_{\text{vibr}}$	=	speed noise introduced by the vibrations of the sensor, m/s
$\delta\nu$	=	linewidth of the backscattered signal, MHz
θ	=	angle of incidence, deg
$\boldsymbol{\rho}$	=	position vector of the measuring volume with respect to the sensor, m
$\boldsymbol{\rho}_{\text{lidar}}$	=	position vector of the sensor with respect to air-data inertial reference system, m
$\boldsymbol{\Omega}$	=	aircraft angular speed (p, q, r), deg /s

Received 24 April 2009; revision received 8 November 2009; accepted for publication 10 November 2009.

*Loads and Aeroelastics Control Engineer, Loads and Aeroelastics, 316 Route de Bayonne, 31060 Toulouse; guillermo.jenaro@gmail.com.

†Senior Expert Optronic Systems, Innovation Works TCC4, Willy Messerschmitt Strasse, 85521 Ottobrunn; nikolaus.schmitt@eads.net.

‡Electronic Systems Engineer, Innovation Works TCC4, Optronics team, Willy Messerschmitt Strasse, 85521 Ottobrunn.

§Optronic Systems Engineer, Innovation Works TCC4, Optronics team, Willy Messerschmitt Strasse, 85521 Ottobrunn.

I. Introduction

FREESTREAM airflow characteristics are valuable information for fixed-wing and rotary-wing vehicles. The forces exerted on the vehicle depend on the relative 3-D airspeed vector, which allows the pilot, aided by the flight-control system, to control the velocity vector of the center of gravity of the vehicle in conjunction with the thrust. Accurate measurement of the airspeed is an essential function for the flight-control system of modern aircraft; this is the reason that they are equipped with sensors to measure this quantity with the highest possible accuracy, commonly using aerodynamic devices such as angle of attack (AOA) and sideslip vanes and pitot tubes. These are capable of measuring the local characteristics of the airflow, which are corrected to give estimates of what the lifting surfaces will experience. The measurement is achieved once the airflow has made contact with the vehicle, which gives limited time (depending on the vehicle geometry and speed) to act in the case of unexpected disturbances coming from diverse sources, e.g., atmospheric instabilities or wake vortices from other flying vehicles.

Remote airflow forward-looking sensing allows new functionalities, due to the extended time available to counteract with the control surfaces. This process can be achieved through a feedforward input to the flight controls of the aircraft. Optimal airload distribution over the wing will alleviate the structural loads and thus allow weight reduction. The generation of counteracting forces will limit the accelerations experienced in the cabin, improving passenger comfort and safety as well as the handling qualities of the flight. Finally, the counteraction against wake vortices could reduce the separation times between takeoffs and landings, therefore increasing the airport capacity, which is one of the major constraints for the growth of air transport [1].

For some of those applications, coherent Doppler lidar devices were suggested. Various U.S. companies and institutions such as NASA and Coherent Technologies, Inc., developed and flight-tested prototypes using infrared lasers at 2 μm [2,3] and 10 μm [4,5], as did some European consortia [6]. More recently, several European programs such as M-FLAME [7] and I-WAKE [8] supported the development of similar systems, and others developed coherent lidar based on a 1.5 μm laser wavelength [9,10]. Some of them have also been flight-tested [5,7,10–17]. However, those approaches are not suitable for reliable onboard detection feeding forward to flight control for automatic turbulence counteraction because of the following problems:

1) The coherent detection requires a narrow linewidth of the received signal and therefore backscatter of the laser pulses by aerosols. However, a sufficiently high aerosol density is not available in all global regions of the world and at higher flight levels, as shown in Fig. 1. Therefore, such a system would not generate signals under all flight conditions.

2) Pulsed coherent systems generate long pulses (type 200–400 ns), mostly at low pulse repetition rates, resulting in a poor longitudinal and temporal resolution.

Such a sensor principle is therefore suitable only for low-altitude operation or applying long integration times for long-range warning systems, but not for safety-critical applications such as feedforward flight control. For a safety-critical feedforward application, the measurement scenario must meet at least the following criteria:

1) A good longitudinal resolution (i.e., the thickness of the air slice measured ahead) is required in the range of approximately ± 10 to 15 m.

2) A forward-looking measuring distance of approximately 50 to 150 m is required to ensure that the measured airflow is the one that actually influences the aerodynamics of the aircraft.

3) An accuracy of 2 to 4 m/s perpendicular to the flight trajectory should be achieved (resulting, for example, in a sensor specification of about 1 m/s along the line of sight (LOS) at an angle of 10° with respect to the aircraft x axis).

4) A temporal resolution greater than 10 Hz is needed.

5) To measure wind speeds perpendicular to the flight trajectory, the sensor must measure at various angles off the aircraft axis.

6) The sensor must be able to produce reliable signals in the absence of aerosols; therefore, it should rely on a molecular backscattering system.

A sensor system that promises to meet these requirements is the so-called direct-detection short-pulse UV Doppler lidar. This new technology is being investigated by U.S. companies [18,19] for very short-range optical air-data measurements and by European consortia for space-based atmospheric missions [20] (with large integration times). Up until now, no airborne systems were presented that are suitable for a feedforward flight control.

This contribution describes the first results achieved in flight tests with a high-resolution direct-measuring short-pulse UV Doppler lidar built to generate data for later coupling with the flight-control system, even at cruising altitudes, where the air is devoid of aerosols. The architecture of this development is described in detail in [21].

A unique lidar onboard sensor was developed and flight-tested using a direct-detection short-pulse UV Doppler lidar. This detection scheme allows measurements even in aerosol-depleted air at distances of 50 m, which is necessary for reliable and high-frequency measurements of clear-air turbulence at cruise altitude. A fringe-imaging technique was used by applying an intensified charge-coupled-device (CCD) camera, allowing fast gating for longitudinal measurement volume reduction (as necessary for real-time control purposes) and in-flight recalibration by image processing. Algorithms have been developed and applied to determine the wind speed at better than 1 m/s accuracy.

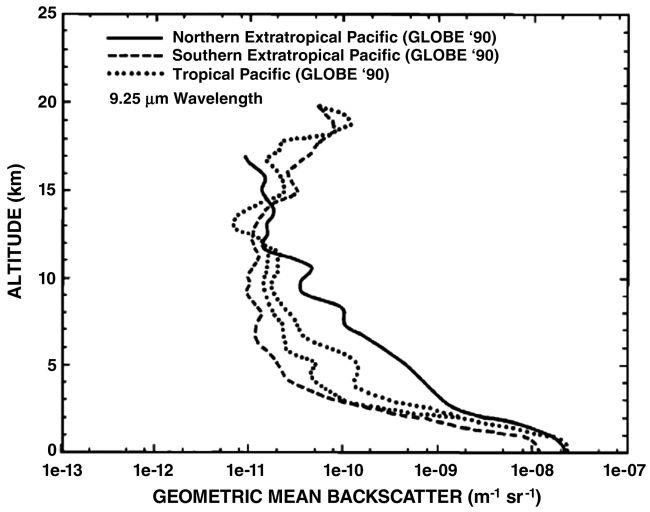

Fig. 1 Altitude versus global aerosol density on the northern, southern, and tropical pacific areas (graph taken from [30]). Data are from 9.25 μm wavelength measurement, but spread of backscatter can qualitatively be transferred to short-wavelength backscatter [31].

II. Onboard Lidar System

A. Load Alleviation

The optimization of the airload distribution over the wing including load-reduction objectives is one of the big challenges of modern aircraft design. Several solutions have been tested and studied in the past, based on diverse architectures, innovative configurations, new control surfaces, next-generation actuators, and new sensors. This paper presents research on a sensor for which the main characteristic is to deliver accurate wind information with phase advance so that the control law would be able to react early enough, to minimize the effect of external disturbances to the aircraft.

The aircraft structure is designed to withstand the loads provoked during its operation. These loads could be divided into two categories: deterministic and nondeterministic. The first category encompasses the loads generated to the aircraft by gravity, inertia, and pilot/electronic flight-control system commands. The second category is due to external atmospheric disturbances, which prompt loads that are nondeterministic, such as the turbulence/gust loads and wake-vortex loads. When flying in turbulence, the local variations of AOA modify the wing lift distribution, thus changing the equilibrium of the aircraft. This phenomenon provokes changes in loads in such a way that they are sizing conditions in some structural components of the aircraft. The Federal Aviation Regulations of the U.S. Federal Aviation Administration and the Joint Aviation Regulations request justification of the structural integrity of the aircraft flying through turbulence.

Figure 2 shows one basic opportunity to compensate the increase in wing-root bending moment that could have been induced by a vertical upward wind. If this wind is known in advance, the flight controller can send a command to, for example, the ailerons to deflect upward. A lead time is necessary, since the angular velocity attainable by the actuators is limited, typically 30 to 40°/s, and the angle of deflection to which the ailerons should be set to maximize the gain can reach 10–15°. This means that the command has to be sent between 200–300 ms before the gust hits the wing [22]. If this

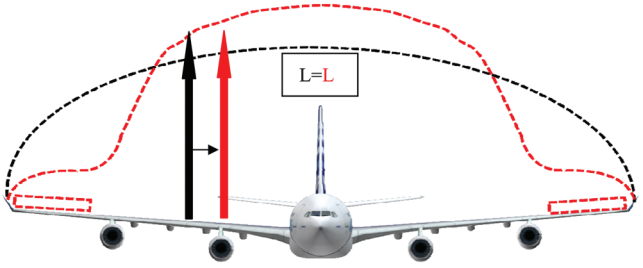

Fig. 2 Wing lift distribution without (black dotted line) with a load alleviation function commanded to outer wing control surfaces. The objective is to move the lift center of pressure inward to reduce the wing-root bending moment in the presence of a gust.

information is provided to the flight controller and the command is sent at the right time, when the gust encounters the wing, the deflection of the aileron will reduce the lift locally. The aircraft needs to be rebalanced to meet the commanded load factor or the 1 g flight. This operation can be included in the design of the control law. This new distribution of lift, moving the center of lift toward the wing root, allows a relief of the bending moment and therefore in the load level that has to be withstood by this structural component. In the end, this will end up in a lighter design and therefore a more efficient and better-performing aircraft.

B. Lidar System

The turbulence sensor aims to measuring airflow dynamics in clear air, which is understood as aerosol-depleted air at high altitudes, as further discussed below. In contrast to systems designed for pilot warning, the sensor described here is designed for direct connection to flight control, allowing the aircraft to automatically and proactively counteract turbulence to minimize their influence on the aircraft, normally done by deflecting control surfaces appropriately. For this, the required preknowledge time is only on the order of 200–300 ms, which is sufficient to feed the information in the flight-control computer and to deflect standard control surfaces up to 10–15 deg in cruise speed. Assuming a cruise true airspeed (TAS) of approximately 250 m/s, the forward-looking range is about 75 m ahead of the wings, resulting in a forward-looking distance of 50 m ahead of the aircraft nose for an Airbus A340-300 aircraft. Note that a significantly longer range (e.g., by an order of magnitude) would not be beneficial, since it would not ensure that the measured volume is the same one that the aircraft will pass through, which is, of course, necessary for real control purpose. Therefore, the sensor technique developed here clearly aims for short- or midrange measurements. However, it could be considered that backscatter from longer distances could be used for other purposes, e.g., for turbulence warning.

The sensor is based on lidar technology [23], incorporating a laser-emitting UV radiation at wavelength λ in the atmosphere, backscattered by particles. The backscattered light is shifted in wavelength by Doppler effect due to the relative movement of the aircraft with respect to the air (TAS). This Doppler shift Δf is measured in a receiver part and is directly proportional to the relative speed v by

$$\Delta f = 2\frac{v}{\lambda} \tag{1}$$

The Doppler speed can only be measured in line of sight; any transversal effects are not accessible to this detection method. Therefore, to determine the full 3-D speed vector, at least three different directions have to be measured, deriving the vertical and horizontal components from speed differences.

The measurement schematic used in this experiment is shown in Fig. 3: Four beams are used, emitted with an angle of 10° vertically and horizontally with respect to the aircraft x axis. The opening angle

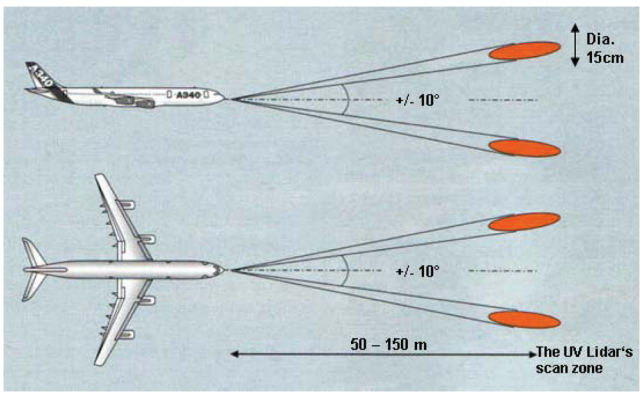

Fig. 3 Beam orientation schematics. Four beams were subsequently emitted under 10° with respect to aircraft axes (left up, left down, right up. right down). Measurement depths are approx. ±15 m from center.

of 10° was considered as a compromise between measurement-point separation and flight-test installation requirements and could be increased for future experiments. The beam diameters are lower than 5 cm, and the measurement volume length is approximately ±15 m from the center to increase the backscatter efficiency. Three beams are necessary to determine the full 3-D vector; the fourth direction is used for increased reliability in case one beam direction is blocked by direct sunlight, if not to increase the accuracy.

The atmospheric backscatter can consist of aerosol particle (Mie) backscatter or molecular (Rayleigh) backscatter. The first backscatter type is very strong in the lower atmosphere, and the backscatter signal is almost not broadened in the scatter process, allowing very precise speed measurements. This scatter is normally exploited in coherent wind Doppler lidar systems. For airborne applications operating in altitudes up to flight level (FL) 400 (which refers to a pressure altitude of 40,000 ft, as FL has been defined as pressure altitude divided by 100) or above, this technique is not suitable for reliable measurements in a given range, as the aerosol density strongly decreases with altitude. This is shown in Fig. 1, in which below about 2000 m above ground, the aerosol density can be quite high, but it varies strongly with meteorological conditions (e.g., long hot periods, just after rain). Above this altitude, the aerosol density decreases drastically, typically by two–three orders of magnitude up to typical cruise-level altitudes in lower stratospheres (FLs 350–510 for transport aircraft). Moreover, as shown in the same figure, a further decrease applies for specific global regions, e.g., for the tropics in the southern hemisphere. Thus, a total spread of aerosol-based backscatter by nearly five orders of magnitude can be observed (or even more, considering extremely high aerosol concentration near the ground in specific conditions) or three orders of magnitude above 2.000 m in height.

In contrast, the molecular backscatter decreases only proportionally to air-density decrease, which results in a factor of roughly 3 from the ground up to the lower stratosphere with no local differences. For this reason, the molecular backscatter gives the more reliable and stronger signal in specific regions or altitudes.

For the reason described, state-of-the-art lidar systems are normally used only in lower-troposphere applications (e.g., for helicopters, as stated in [9,10]), or they need seeding of the air by artificial aerosols such as smoke [24] for higher-altitude applications.

The lidar used here is another kind: the so-called Rayleigh type of lidar based on the molecular backscatter. Nevertheless, if aerosol backscatter is present, this signal will be exploited together with the molecular signal, whereas in a situation with no aerosol backscatter, the molecular signal is still very strong. This technology implies two consequences: First, as Rayleigh backscatter coefficient β is proportional to the reciprocal of the wavelength approximately to the power of 4, a laser should be used with the wavelength as short as possible:

$$\beta(\lambda) = \left(\frac{\lambda_0}{\lambda}\right)^{4.09} \times \exp\left(-\frac{z}{z_0}\right) \times 10^{-9}\,\frac{1}{\text{cm}\cdot\text{sr}} \tag{2}$$

where λ is the laser wavelength in nanometers, z is the altitude in kilometers, λ_0 is the reference wavelength of 1064 nm, and z_0 is the reference altitude of 8 km. The factor 4.09 in the exponent differs from the pure molecular backscatter factor of 4, due to dispersion of the refractive index of the air [25].

Second, due to the Brownian thermal motion of the molecules causing Doppler broadening $\delta\nu$ of the molecular backscatter line itself, resulting in about a 2-GHz-wide backscatter line (see Fig. 4), even if a narrow laser beam is emitted, the coherent heterodyne detection scheme used in state-of-the-art Mie lidar cannot be applied to this very broad received signal:

$$\delta\nu = \frac{1}{\lambda}\sqrt{\frac{8\cdot k_B\cdot T\cdot \ell_n 2}{m}} \tag{3}$$

For a temperature $T = 220$ K with a molecular mass of air m of about 28.96. $\times$ 1.66 $\times$ 10^{-27} kg, the linewidth $\delta\nu$ is about 1,67 GHz,

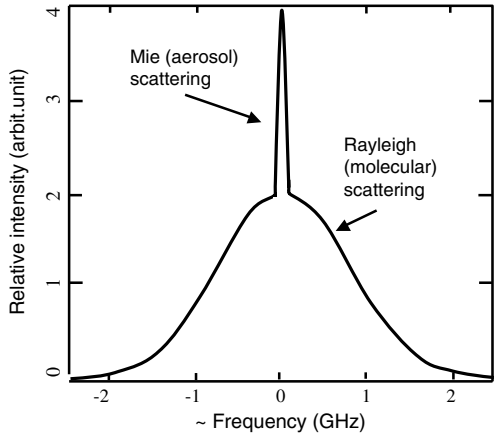

Fig. 4 Schematic sketch of backscatter signal intensity (arbitrary units) versus signal frequency. The Mie scattered signal exhibits nearly the same linewidth as the emitted laser line, whereas the Rayleigh (molecular) signal is strongly broadened to GHz range due to the high Brownian particle speed inducing Doppler broadening.

corresponding to a molecular speed of ± 148 m/sπ, where λ is the laser wavelength, and k_B is the Boltzmann number.

In the applied so-called direct-detection scheme, a frequency- or wavelength-discriminating device is needed to determine the Doppler shift. In the presented case, a Fabry–Perot interferometer and a fringe imaging technique are used [26]. The required velocity accuracy of about 1 m/s for the detected signal corresponds to a frequency shift of approximately 5.6 MHz at the selected UV wavelength of a signal with a spectral width of approximately 1.67 GHz, which corresponds to a full-width Doppler broadening of 296 m/s. Therefore, the frequency shift of the entire detected broadband signal has to be measured with a relative precision of about 1/300. The overall system architecture is shown in Fig. 5.

A laser generates a single-frequency UV beam at 355 nm, delivered through transmitter optics and transmitted as a highly collimated (parallel) beam with less than a 5 cm (typically about 2 cm) diameter into the atmosphere, multiplexed into four directions successively. Atmospheric backscatter is collected by the same optics with a directional multiplexer and delivers Doppler-shifted light to the receiver, incorporating a Fabry–Perot interferometer. The interferograms are imaged by an intensified charge-coupled-device (ICCD) camera for which the images are digitally transmitted to a data recording and preprocessing electronics. Each of those main components is characterized in detail below.

The laser used is an amplified pulsed single-frequency neodymium-doped yttrium-vanadate (Nd:YVO_4) laser, diode pumped, with a repetition rate of 18 kHz and a pulse length of about 8 ns. The infrared Nd:$YVO_4\eta$ emission wavelength of 1064 nm is frequency-tripled into 355 nm radiation (UV region) to increase the Rayleigh backscatter efficiency. The average output power is 3 W in UV. Since such a laser was not commercially available, it has been developed and built within the frame of this project.

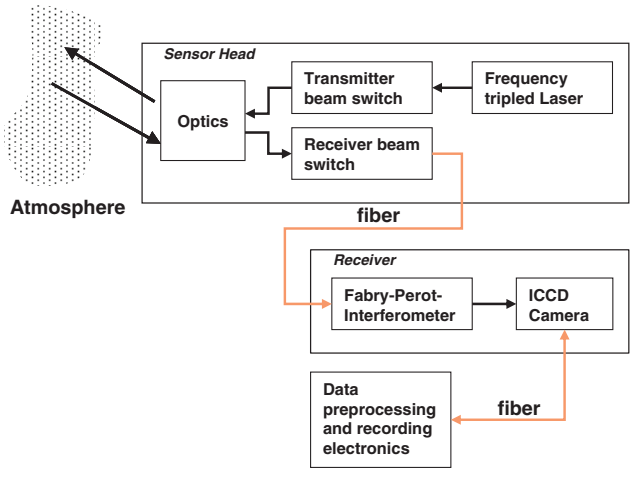

Fig. 5 Overall lidar system architecture.

This laser is eye-safe only at certain minimum distances from the emitter, depending on the exposure time to the human eye. For short exposure times of 0.25–2 s, the minimum distance to guarantee eye safety is 15.8 to 34.8 m, respectively, or 63 m for 10 s of exposure. It is assumed that no person will be within that distance from the aircraft during flight operation; thus, the laser can be safely operated during flight. For longer exposure times, this minimum distance increases to 200 m for 100 s and to 632 m for 1.000 s. For flight operations, this is not relevant, as such long exposure times for relatively small, parallel beams in moving conditions can be considered as impossible; however, for ground operations, this must be considered. As a consequence, the lidar may be operated on the ground in static conditions only when it is guaranteed that no person without appropriate safety instruments (laser goggles) can be within that distance. The appropriate safety measures can be guaranteed for maintenance, but not for ground operations of the aircraft. For that reason, the lidar was in operation only when an interlock switch built by hard electrical wiring, which connected to the landing gear, was closed; i.e., as soon as the landing-gear switch was active, the lidar was shut off. In future operations, this landing-gear interlock could be replaced by a more appropriate on-ground sensor switch, e.g., the one commonly used for thrust inversion enabling.

The optics are designed and built specifically to the sensor needs, including a 20-cm-diam collector front lens, used for transmission and reception beams simultaneously (collinear design). The laser beam is switched between the four measurement directions, with switching times well below 1 ms, using a patented rotating-prism design [27]. The receiving beams from all four measurement directions are collected by the same front optics, but then focused by four separate focusing optics into optical fibers, which are concentrated in a 4:1 multiplexer afterward, synchronized with the transmission-beam switch. The optical-head optical-fiber output therefore sequentially delivers the Doppler-shifted backscatter signal of the four measurement directions into the receiver.

Within the receiver, the fiber output is collimated and sent into a Fabry–Perot interferometer, for which the so-called finesse and free spectral range parameters were optimized for Rayleigh detection. The Fabry–Perot interferometer consists of two plan-parallel optically coated surfaces, allowing multibeam interference of the parallel received beam. The optically coated parallel surfaces generate constructive optical interferences by multibeam interference of phase-synchronous light beams bouncing back and forth, whereas antiphase-synchronous light beams generate destructive optical interferences. All constructive and destructive interferences display circular symmetry with respect to the beam center, as phase differences between adjacent beams are a function of the sine of the angle with respect to the optical axis. The shift of the radius of those fringes with respect to the fringe radius of the transmitted light is directly proportional to the Doppler shift of the backscattered light. At every eighth measurement, the direct laser beam was coupled to the transceiver to determine the unshifted laser fringe diameter, and Doppler shift was then directly calculated from the fringe-radius difference of backscattered-vs-transmitted laser radiation. The laser does not therefore need to be stabilized, as drifts are very slow in comparison with these reference-beam fringe-radius updates and are therefore fully compensated.

The Rayleigh backscatter signal and the Mie backscatter signal generate the same types of fringes, only differing by their typical widths. Thus, in the case of strong Mie backscatter (in clouds, at low altitudes), this signal increases the signal-to-noise ratio of the detection, whereas in a pure Rayleigh detection regime (at high altitudes, in clear air), the molecular signal still is sufficient to determine the speed with desired accuracy. The interferograms, consisting of circular high- or low-intensity fringes (see Fig. 6), are registered by an intensified CCD camera.

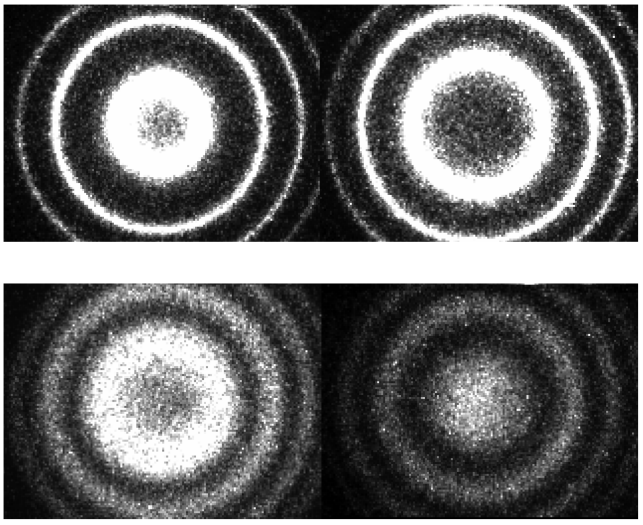

Fig. 6 Measured interferograms. Upper left: reference signal (emitted laser); upper right: backscatter in dense clouds (nearly pure Mie); lower left: backscatter at 12,000 ft altitude; and lower right: backscatter at 39,000 ft altitude (nearly pure Rayleigh).

The intensifier used is a microchannel plate with a front cathode, specifically sensitive to UV light, in which free electrons are generated and accelerated by the microchannel-plate amplification voltage, now able to generate many photons by one accelerated electron in the phosphor coating of the other side of the microchannel plate. The microchannel plate is used for three functions by the same element: first, conversion of UV light into the visible spectrum adapted to CCD sensitivity; second, amplification of the received signal; and third, fast switching (gating) of the receiver sensitivity.

The measurement process is synchronized as follows: The laser transmits a beam at given time t_o and delivers a trigger signal to the receiver electronics. The receiver electronics switches the microchannel plate into the sensitive regime after a time t_1, which is defined by the time that the laser beam has reached the beginning of the measurement volume. In our case, measurements shall be taken at 50 m distance ± 15 m measurement depth. Considering a light propagation time of about 3 ns/m (which is 6 ns/m in backscatter), the receiver is switched to sensitive after 210 ns and to insensitive after 390 ns. In this way, the measurement volume is defined by the switching of the receiver with respect to the transmitted laser beam propagation.

The CCD camera is operated at a 60 Hz frame rate, updating the measurements with the same rate, allowing 16 ms of exposure time per frame. To increase backscatter efficiency, about 300 laser pulses can be integrated into a single measurement frame. Actually, the number of measurement pulses received is dynamically switched with respect to backscatter intensity, allowing an increase of overall receiver dynamics as necessary, e.g., in the case of flying through clouds with strong Mie scatter.

The fringe images registered by the CCD camera are delivered over a fiber-optical data link to the data recording and preprocessing electronics, consisting of a free-programmable gate-array-based architecture for preprocessing and data splitting and a hard-disk array for recording. Preprocessing includes dynamics control (number of integrated laser pulses per frame) and the determination of other parameters for sensor control. In the next step, the full data processing shall be implemented.

Various attempts are reported in the literature to evaluate the fringes of such interferograms. For real-time purposes, it is desirable to transform the images into a 1-D format, taking into account the aperiodic behavior of the fringe function. Others have developed an optical solution [28]. In contrast, we have used an effective digital new method, suitable for highly parallel processing. The algorithms were developed in several stages, ending up with the desired accuracy and a speed of only about 12 times slower than needed for real-time processing; thus, the next step of implementing this in real-time hardware and achieving full real-time processing seems very realistic.

The fringe images were analyzed postflight by specifically developed algorithms. They form a radially symmetric intensity distribution called the Airy function:

$$I(\lambda,\theta)=\frac{T_r^2}{(1-R^2)}\left(1+\frac{4R}{(1-R)^2}\cdot\sin^2\left(\frac{\vartheta}{2}\right)\right)^{-1} \tag{4}$$

with

$$\frac{\vartheta}{2}=\frac{2\pi n_{\text{gap}}h\cdot\cos(\theta)}{\lambda} \tag{5}$$

where I is intensity (W/m^2), λ (nm) is the wavelength, T_r is transmission of the resonator, θ is the beam angle with respect to the optical axis, R is the reflectance of the resonator surfaces, h is the distance between the two resonator plates (gap), and n_{gap} is the index of refraction thereof.

The circle radius at given wavelength λ can be derived from θ. In practice, this function must be modified, because the thermal broadening due to the Doppler shift caused by the Brownian motion has to be considered. This implies the convolution of the intensity $I(\lambda,\theta)$ with the Gaussian distribution of the one-dimensional speeds of the scattering particles, taking into account the mixture of molecules and aerosols. Also, artifacts of the optical system, such as a decrease of image brightness at the periphery of the image (vignetting) and an offcenter beam-axis position, must be modeled. The resulting function is quite complex: in brief, it contains parameters describing the position of the maxima of the rings (with the width of the rings depending on the air parameters) and parameters modeling the optical artifacts.

Those fringes of circular symmetry are much broader than the pixel size in the optical design used here and are imaged with a rectangular array of light detectors (pixels), such that the decline of a circle is detected at an adjacent pixel by different intensity fractions. Since they are forming a continuous radial-symmetric intensity distribution, the peak of the function can be determined very well with a limited number of samplings (detector pixels), as long as the fringe-intensity distribution is known very well, which was physically modeled in detail and included in the detection algorithm. As a result, the fringe radii were determined in this system with a resolution of about 1/50 of a CCD pixel.

Figure 7 shows the optical-head hardware (including laser, multiplexers, and optics), and Fig. 8 shows the receiver (including transfer optics, Fabry–Perot interferometer, and ICCD camera). The data recording and preprocessing electronics are shown in Fig. 9. All parts were not intended to be realized in a miniaturized way, as only physical feasibility proof was intended. For future aircraft integration of such a system, a miniaturization will be needed.

The lidar sensor was realized in two phases. In stage 1 a flight-worthy system was built to be capable of looking ahead 35 m to prove

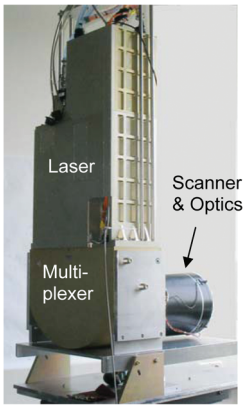

Fig. 7 Sensor head including laser (upright box), multiplexers (lower box), scanners, and optics (horizontal black cylinder).

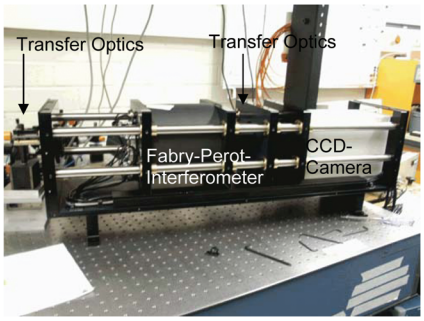

Fig. 8 Receiver, incorporating the Fabry–Perot-Etalon and the ICCD camera.

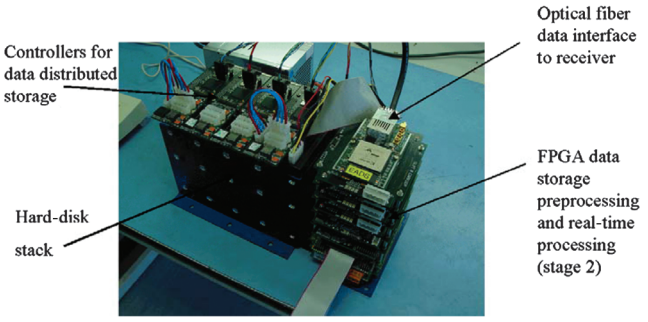

Fig. 9 Data preprocessing and recording electronics, with main functional units indicated (FPGA denotes the free-programmable gate array).

the feasibility of the principle. This was flight-tested in 2004, and the results have been reported in [29]. Stage 2 of the system, for which results are reported here, was flight-tested in 2006; in addition to stage 1, it consists of an upgraded laser at 10 times the output power and more than 10 times the optical receiver efficiency.

The sensor head is shaped like a L, due to the aircraft integration constraints. As the A340-300 test aircraft should not be mechanically modified too heavily, it was decided to place the optics in a fairing outside the standard aircraft skin below the cockpit. The L shape of the sensor head allowed mounting through a maintenance door of the front avionics bay, with the optics part being placed in the fairing and the laser part extending into the avionics bay (see Figs. 10 and 11). The receiver was mounted inside the avionics bay. The power supply and control were installed separately in the cabin.

Ground tests have been performed in a laboratory using a rotating disk as reference. The laser beam and receiving optics were tangentially directed to the disk border, and the disk was rotating at a measured speed of about 180 rps with a corresponding track speed of

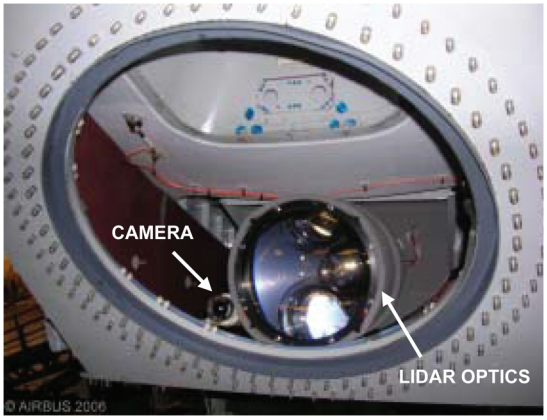

Fig. 10 Lidar optics inside the fairing. The small optical lens on the left belongs to a standard video camera for window monitoring.

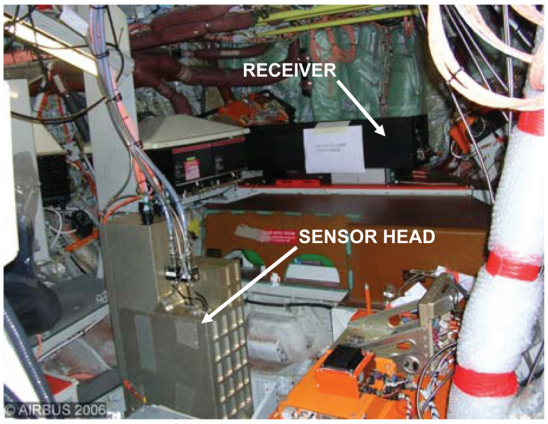

Fig. 11 Sensor-head upper part inside the avionics bay, with the receiver placed in the front of the bay.

66 m/s. The absolute errors measured were about 1 m/s, and standard deviations were below 0.2 m/s for the reference signal. The measurement channels were analyzed in two modes of the receiver: a high-sensitivity mode and a low-noise mode. In the low-noise mode, the achieved standard deviation for the measurement channels was between 0.44 and 0.55 m/s, and in the high-sensitivity mode, it was between 0.49 and 1.12 m/s for three well-aligned channels. As the high-sensitivity mode already fulfilled the targeted specification, this mode was chosen to ensure best results for the full flight envelope.

C. Lidar Installation in the Aircraft

The solution chosen for the system installation on the aircraft is an L shape for the optics, so that the forward-looking configuration is feasible without the need of additional mirrors. The optics head remains outside the testbed, with the center in line with the aircraft's x axis; thus, the four measurement directions were 10° off of the aircraft's x–y and x–z planes, or 14° off of the aircraft's x axis. It is covered with a fairing designed to minimize the impact on the airflow (see Fig. 12). The fairing shape is kept by means of an inner structural box, which is also in charge of withstanding the pressure difference, as the sensor is hosted in a pressurized zone. Not much effort is put on this exercise, since this solution is only for the current flight tests of the system and not for an industrial solution. Figure 13 shows the fairing below the aircraft nose, the position of which was chosen for maximum forward-looking range and minimum impact of aircraft banking, as well as for minimum dynamics of the structure.

To minimize the impact on the flying testbed, the rest of the optics is hosted in the electronics bay area so that a maintenance door can be used. The local structure of the testbed is reinforced to ensure the required level of safety following Airbus standard procedures.

The fairing embeds the UV transmissive window with anti-reflection coating for the laser wavelength. The fairing is also equipped with an active system to prevent the condensation of water in the window, based on the generation of a dry airflow that sweeps the window.

For a future aircraft implementation, it will be necessary to integrate the lidar skin conformally into the aircraft. A preferred position for the optical sensor head will be the radome, as it is the most forward part of the aircraft, which then has to be equipped with a window. Bird strike and flashing topics are expected to be solvable using existing technologies for aircraft windows; additionally, heating has to be applied to prevent icing. The technology of pulsed direct-detection lidar used here is very insensitive to local contaminations. Other installation locations can be considered, but they exhibit drawbacks in terms of backward position (reducing the forward-looking distance). Furthermore, it has to be ensured that the installation section is not vibrating or moving with respect to the aircraft, as the measurement is a relative one and such vibrations or movements then have to be compensated. All other components of the lidar (e.g., remote laser parts, receiver, electronics, and data processing) can be

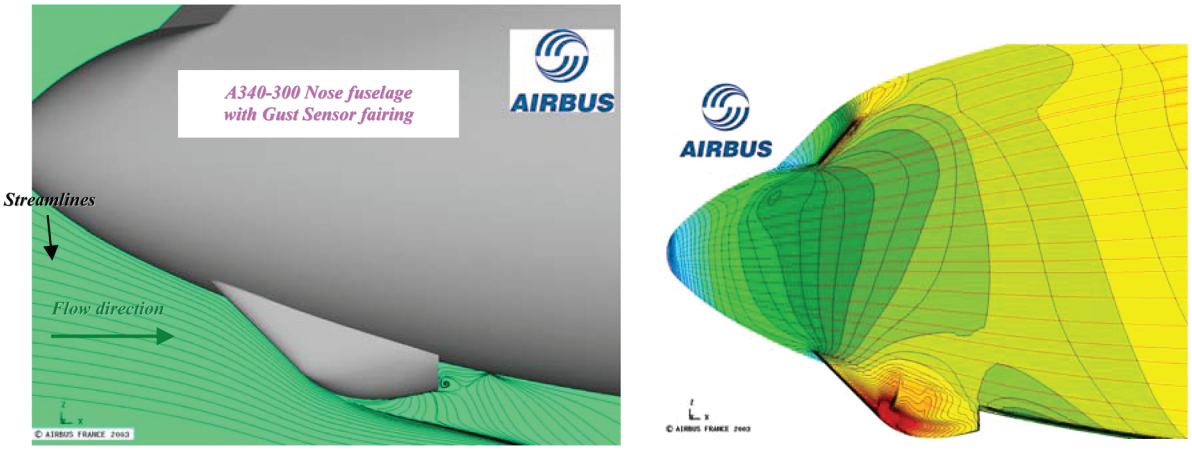

Fig. 12 Aerodynamic study of the flow development (left) and the pressure distribution around the fairing for $M = 0.82$, $\alpha = 0°$ $\beta = 0°$, and $Re = 47 \times 10^6$, fully turbulent flow.

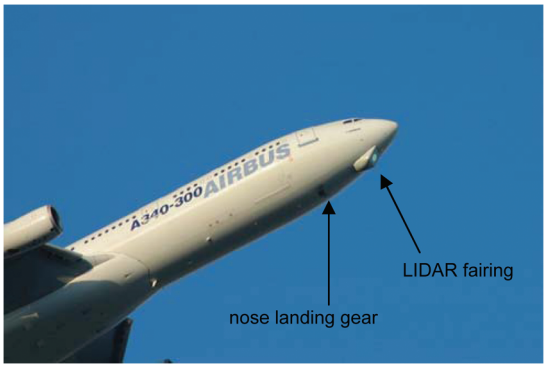

Fig. 13 Structural box completed with aerodynamic fairing below the A340 nose.

installed remotely in an electronics bay. Depending on application and related safety standards, it might be necessary to install two redundant lidar systems. As this lidar system will be directly connected to flight control for automatic feedforward, it is expected to be a separate system apart from pilot assistance systems such as enhanced-vision systems and synthetic-vision systems, even though the information of the lidar can be fed as input information into such assistance systems. If longer-range measurement functions can be integrated or if lidar data additionally becomes an integral part of enhanced-vision systems and synthetic-vision systems situation-awareness information, this might be subject to change.

D. Aircraft Movement Compensation Algorithm

Since the sensor's measurement is relative to the sensor's position, its own movement is included in the output of the gust, and this must therefore be compensated to measure the atmospheric perturbations such as turbulence. Basically, the aircraft's motion data are transferred from the computer unit onboard for flight control and are fed into the equation (see Fig. 14)

$$V_{\text{compLOS}} = (\boldsymbol{V}_{A/C} + \boldsymbol{\rho}_{\text{lidar}} \wedge \boldsymbol{\Omega} + \Delta \boldsymbol{V}_{\text{vibr}}) \cdot \frac{\boldsymbol{\rho}}{|\boldsymbol{\rho}|} \tag{6}$$

$$V_{w\text{LOS}} = V_{\text{LOS}} - V_{\text{compLOS}} \tag{7}$$

where V_{compLOS} is the aircraft's motion-induced speed to be compensated, $\boldsymbol{V}_{A/C}$ is the aircraft translational speed, $\boldsymbol{\Omega}$ the aircraft rotational speed (p, q, r), $\boldsymbol{\rho}$ is the position vector of the measuring volume with respect to the sensor, $\boldsymbol{\rho}_{\text{lidar}}$ is the position vector of the sensor with respect to the velocity known point [often from the air-data inertial reference system (ADIRS)], $\Delta \boldsymbol{V}_{\text{vibr}}$ is the noise brought in by the vibrations of the sensor, $V_{w\text{LOS}}$ is the turbulence wind speed projected onto the LOS of the lidar measuring directions, and V_{LOS} is the LOS measured speed.

Because the Doppler lidar sensor measures TAS, it is a relative measurement of aircraft movement with reference to the surrounding atmosphere. Although an appropriate measurement system in turbulence is lacking as a reference of turbulence-speed vector determination, the aircraft was flown in a controlled stabilized condition, generating reproducible relative airflow referenced by the calibrated ADIRS, and both data were compared. Thus, the terms compared for

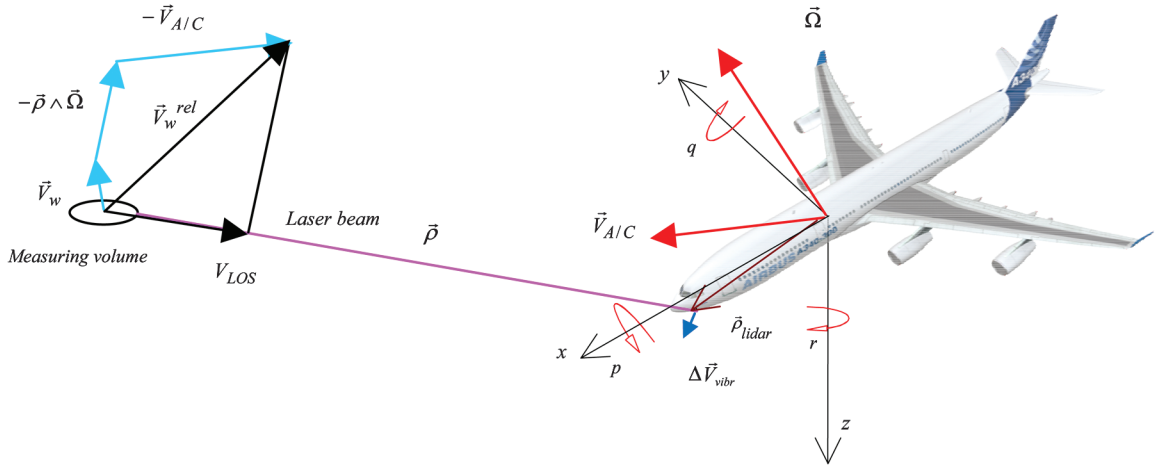

Fig. 14 Sketch of a flying A340-300 aircraft equipped with a lidar. The speed measured by the system includes the motion of the aircraft.

the validation of the sensor measurements are those of Eq. (7) in low turbulence and therefore have a negligible wind speed.

The three components of the velocity vector are derived from the four LOS measurements, applying the orthogonal projection method. This provides the best approximation in the least-squares sense.

Grouping together the four equations for the four LOS directions,

$$\{V_{w\mathrm{LOS}}\} = U^e\{V^e\} \tag{8}$$

where U^e is a matrix, for which the columns contain the components of the unitary vectors aligned with each of the LOS directions in a given reference frame, and $\{V^e\}$ are the three components of the airspeed given in the same reference axes. Thus, the best approximation for the wind $\{V^e_{\mathrm{ap}}\}$ in the standard error (least-squares difference) is given by the solution of the following equation:

$$U^{e^T}\{V_{w\mathrm{LOS}}\} = U^{e^T}U^e\{V^e_{\mathrm{ap}}\} \tag{9}$$

.

III. Flight Tests

Several flight tests with a total duration of more than 17 h were performed. Different flight envelopes (altitude/speed combinations) including flight levels up to FL 390 [see Fig. 15, in which deviations from constant flight levels are due to specific maneuvers performed at several FLs, e.g., constant sink rate and constant α (see below)], and speeds up to Mach 0.82 were covered. The weather conditions varied from clear air to dense clouds at various altitudes. The flight-test envelop included stabilized level flights at constant speeds up to FL 390 (maximum achievable flight altitude), with short intermediate testing periods of constant-alpha flight, constant descent at $\alpha = 0$, and descent at constant rate of descent and constant vertical acceleration. At maximum flight level, two sets of 360° heading sweeps were flown to measure the solar background and signal-to-noise ratio with the laser switched off and on again. The result is shown in Fig. 16. To better demonstrate the differences, the heading direction is given between approximately −80 and +780°, not solving the ambiguity.

Between 100 and 460°, the laser was shut off. The backscatter signal was nearly a factor of 4 above the background, and at approximately 230°, a slightly increased background was registered due to the sun direction, increasing background light by no more than a factor of about 1.5. This can be seen again at approximately 590°, when the backscatter signal was only very slightly disturbed. It is therefore proven that the backscatter signal lies well above background and the sun has no major influence, which was achieved by properly gating the detector to be sensitive only within the measurement volume and with the usage of adequate daylight filters. Nevertheless, during the full flight period, it could not be ensured that the optics were not directed into very direct sunlight. To protect the

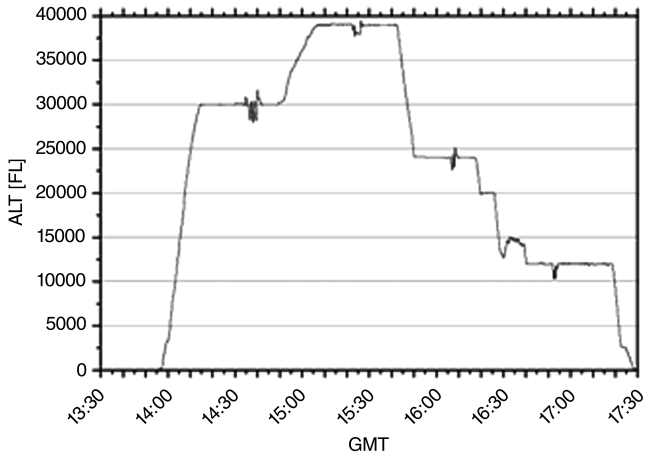

Fig. 15 True altitude versus time of the full flight-testing envelope (GMT denotes Greenwich Mean Time).

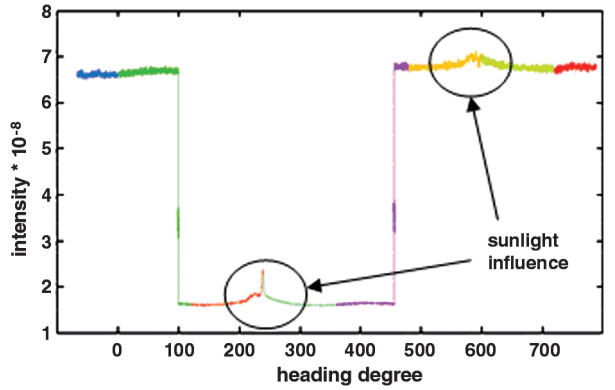

Fig. 16 Two full curves flown with the aircraft at FL 390 to measure atmospheric backscatter, with signal intensity plotted versus (ambiguity not resolved) aircraft heading: lidar receiver signal with laser on (−50 to 100° and 460 to 780°) and laser off (pure atmospheric backscatter from 100 to 460° heading). The small sunlight influence can be seen at 230 and 590°.

detector, the detection path was interrupted in such cases by the help of sun sensors included in the optics. Note that such a cut down of one of the measurement channels for a short time was observed several times, but it was not proven that not shutting down the receiver would have led to damage. As four instead of three necessary measurement directions were realized, the loss of a single channel for a short time by sensor-induced shutdown did not influence the usability.

In Fig. 6, recorded fringe images are shown for the reference signal, dense clouds (nearly pure Mie regime), FL 120, and FL 390 (very clear air, nearly pure Rayleigh regime). It can be clearly seen that the fringe contrast is still very good even at maximum altitude. More remarkable is the narrower fringe width that can be seen from the pure Mie-regime cloud backscatter in comparison with the wide Rayleigh-regime backscatter at maximum altitude.

Typical speed measurements are shown in Fig. 17; the four lidar measurement curves (noisy curves) of the four directions are upshifted by 20 m/s to be able to separate them visually. Also included are the aircraft reference-speed curves (TAS projected to the lidar line of side speeds), upshifted the same way (smooth curves). The aircraft reference measurement system (pitot-tube based) was calibrated in the former flight using trailing cone sensors, etc., thus guaranteeing a high level of precision. Lidar and aircraft reference curves show the same dynamics (with lidar data being a bit more noisy, as unfiltered values are plotted) and lidar speeds exhibit differences with respect to aircraft reference values. It was found that these differences are due to optical aberrations in the transfer optics of the receiver. Figure 18 shows the same measurement with optical aberrations compensated systematically, now exhibiting very good coincidence of lidar and aircraft-speed values and again displaying excellent equality of dynamics. The noise in the plotted data is

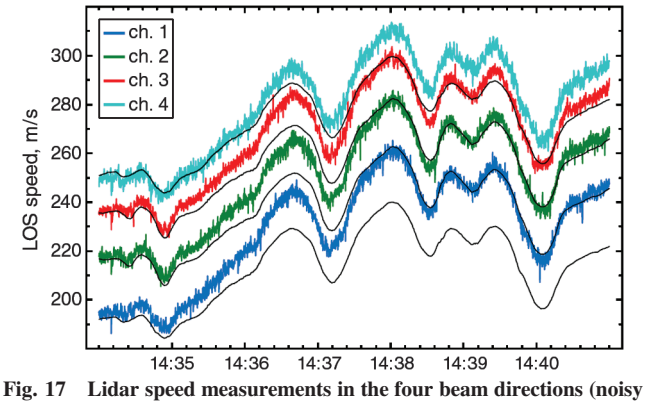

Fig. 17 Lidar speed measurements in the four beam directions (noisy curves), upshifted by 20 m/s for better visibility, and aircraft reference speeds in the same measurement directions (smooth curves), upshifted the same way, before optical aberration compensation.

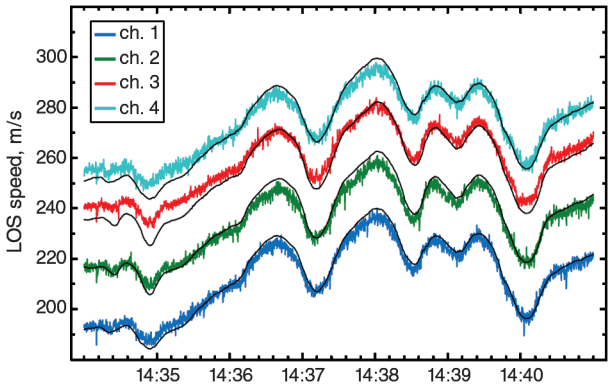

Fig. 18 Same as Fig. 17, after compensation for optical aberrations.

generated by photon-count-dependent shot noise (as instrument noise was found to be slightly lower in ground tests) as well as noise caused by atmospheric effects, which cannot be determined (discussed below).

In Fig. 19 the differences between lidar measured speeds and aircraft reference speeds are plotted versus time for the full flight test. There are some major differences in the aircraft start phase (approximately 14:00 hrs); further, some very short-time differences occur. The gap at approximately 15:15 hrs indicates the period in which the laser was shut off for the background measurements described above; thus, no valid data have been recorded. In general, the speed differences are on the order of 5 m/s, which is quite a good value. The larger errors indicated in the start phase have to be further analyzed; however, for turbulence measurements, only dynamic changes have to be registered. In Fig. 20 the standard deviation of one of the measurement channels is shown. This standard deviation is plotted for the full flight-test time again, including all phases of changes in aircraft motion. For evaluating the estimated standard deviation of the instrument, only the phases of constant flight should be evaluated. Furthermore, the flight phase at maximum altitude is especially of specific interest, which is highlighted by a box in Fig. 20. It is shown that the standard deviation was approximately 1.3–1.5 m/s most of the time.

Because of decreasing temperature in the avionics bay, cooled by the reduced thermal insulation of the fairing, the laser power dropped down during the flight test (see Fig. 21 for laser temperature and Fig. 22 for laser output power). This is the reason that the standard deviation in the second half of flight test at lower altitudes is larger than in the first half at the same altitude. However, during the FL 390 maximum-altitude test period, the laser power was still nearly unaffected. Also note that the standard deviation includes all atmospheric phenomena, which are not registered by the onboard aircraft-speed measurement system. Any real measured turbulence at the measurement distance (which is not registered by the calibrated

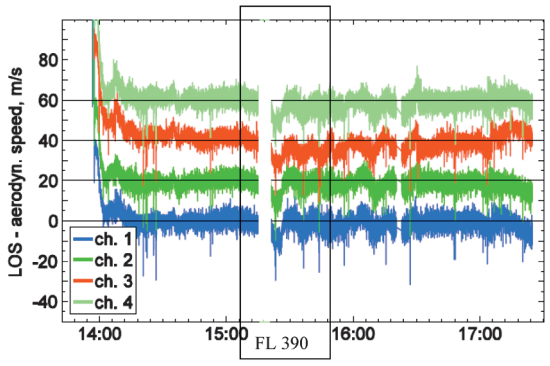

Fig. 19 Unfiltered differences between lidar speed (TAS) measurements in the four beam directions (noisy curves) and aircraft reference speed (TAS) projected to the lidar measurement directions, upshifted by 20 m/s for better visibility.

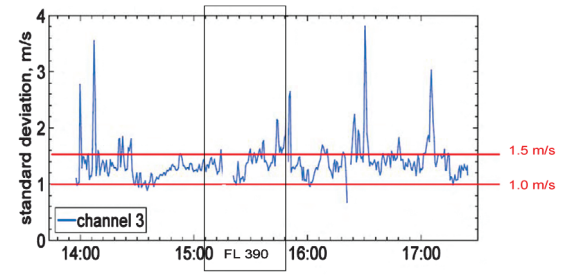

Fig. 20 Standard deviation of one measurement channel over full flight-test period. The most interesting period at altitude 39.000 ft is indicated.

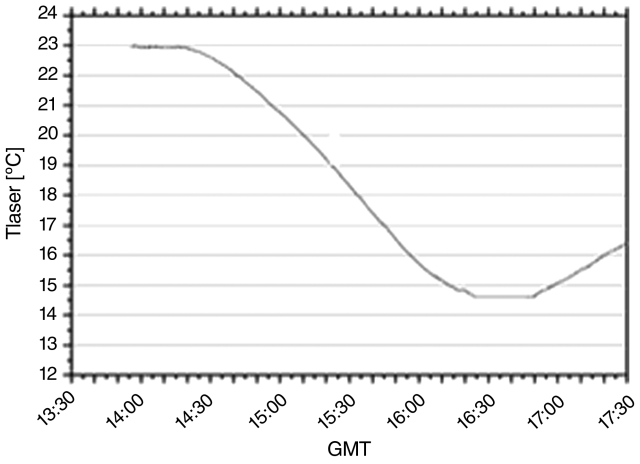

Fig. 21 Temperature drop of laser due to avionics-bay temperature decrease during the flight test.

onboard airspeed reference system, due to the fact that either this turbulence is modified when entering the reference system or it has higher dynamics than the reference system) is interpreted here as noise. Thus, the given values for the standard deviation are worst-case noise values, and real noise-based standard deviation is expected to be smaller. However, due to the lack of a comparable reference-speed measurement system, the actual noise value cannot be assessed, and it cannot be determined if the spikes in the standard deviation diagram shown in Fig. 19 are due to atmospheric phenomena such as turbulence or not (especially since the deviations are quite small).

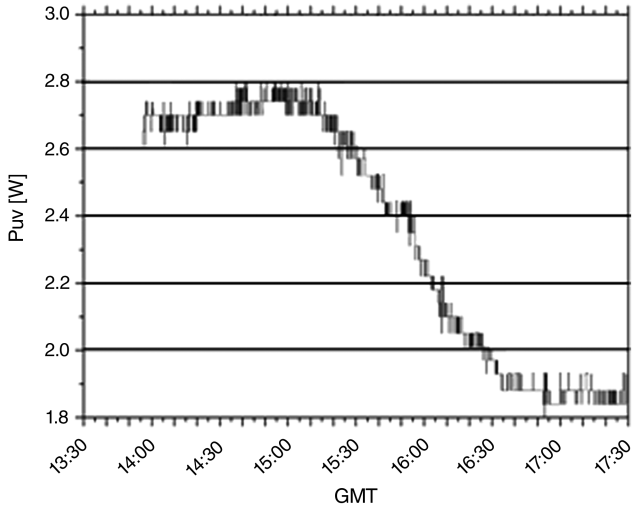

Fig. 22 Drop of laser power during flight test due to temperature decrease in the second half of the flight test.

Horizontal- and vertical-speed components are derived from speed differences of two measurement beams; horizontal components are derived as differences from the two lower beams and differences of the two upper beams, and vertical components are calculated from differences of the two left measurements and differences of the two right measurements (see Fig. 23).

Figure 24 shows such differences in a flight period in which sinking and climbing were performed. The upper two curves display the horizontal components, and the lower two curves display the vertical components. All curves are shifted by 20 m/s to each other for better optical display. The noisy curves are the lidar measurements, and the smooth curves are the aircraft reference data and were calculated in the same way. In this unfiltered data, a good coincidence of the lidar data and the aircraft measurement data can already be seen in the sinking/climbing periods of, for example, 14:35:00 and 14:38:30 hrs and in other periods for the lower two curves (vertical components). This coincidence can be made visible in a better way using filtered lidar data, as shown in Fig. 25, showing the same measurements, but lidar data were filtered at 0.25 Hz. Again, the coincidence of lidar and aircraft data in the aforementioned periods and further periods can be seen for the vertical component. Note the overall small vertical speed in sinking/climbing of a maximum of 2–5 m/s, which is well-detected and measured.

For the horizontal component, the aircraft performed changes in sideslip angle (beta) in another flight-test period, shown in Figs. 26 and 27. Here, the coincidence between lidar and aircraft data can be seen, for example, between 15:10 and 15:40 hrs in the upper two curves (horizontal components). Figure 26 displays unfiltered lidar data, and Fig. 27 displays lidar data filtered at 0.25 Hz.

In Fig. 28 the standard deviations of the vertical (lower curve) and horizontal (upper curve) speed differences are plotted, showing about 1.5 m/s standard deviation again at the maximum flight level (and the already- discussed higher values for the second half of the flight test than for the first half). This standard deviation represents the differences of speeds measured in the upper and lower beams. The projection to the perpendicular aircraft axes needs a multiplication of the speeds and the standard deviation by a factor of $\cos(\varphi)$, where φ represents the beam angles versus aircraft horizontal datum x; with φ at 10° in our case, this factor is 2.9. Thus, the standard deviation of 1.5 m/s has to be multiplied by 2.9 to result in the standard deviation in aircraft y and z axes. For a future system, θ therefore should be increased (which was not possible here, for mechanical reasons) to have nearly uniform standard deviations in all three aircraft axes.

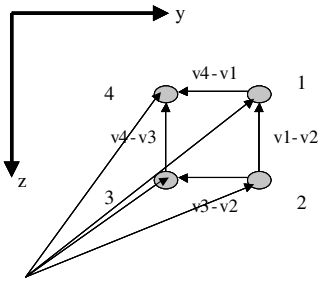

Fig. 23 Calculation of vertical and horizontal speed components as differences of line-of-sight speeds measured in the four beam directions.

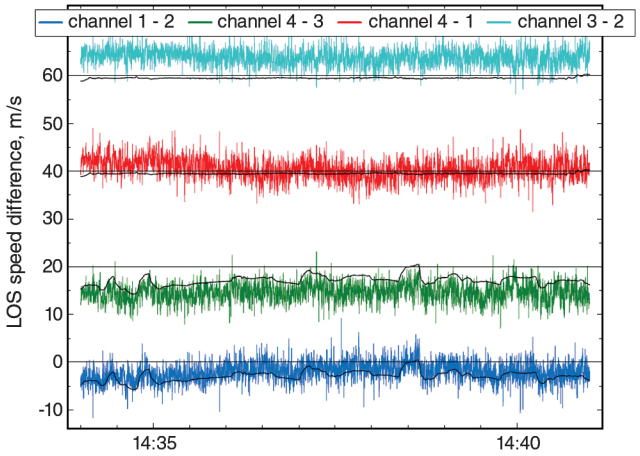

Fig. 24 Flight-test period with constant rate of descent and climbing rate, generating relative vertical components as shown in the lower two curves. Noise curves show lidar data. All curves are upshifted by 20 m/s for better visibility.

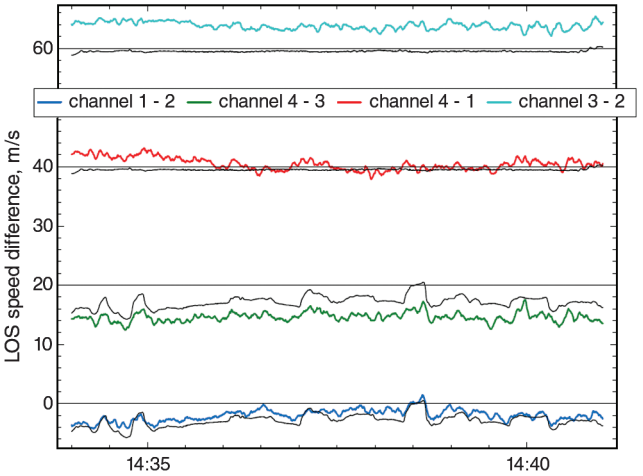

Fig. 25 Same as Fig. 24, but with lidar data filtered at 0.25 Hz.

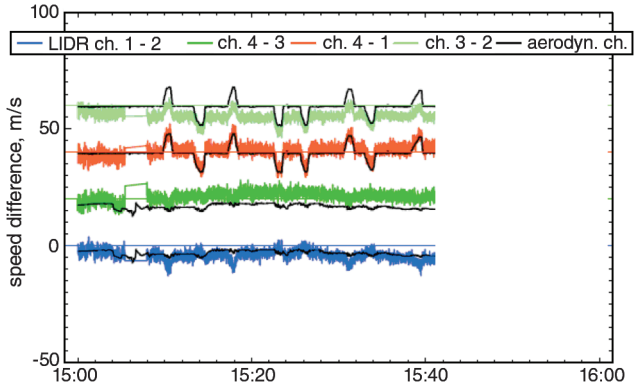

Fig. 26 Same curves as Fig. 24, but with in-flight testing of beta changes of the aircraft, leading to horizontal relative speed components.

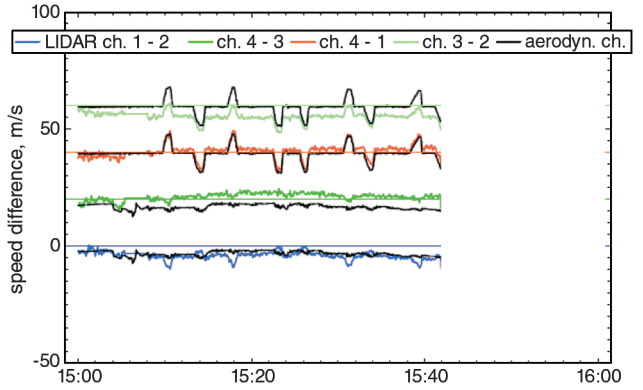

Fig. 27 Same as Fig. 26, but filtered at 0.25 Hz.

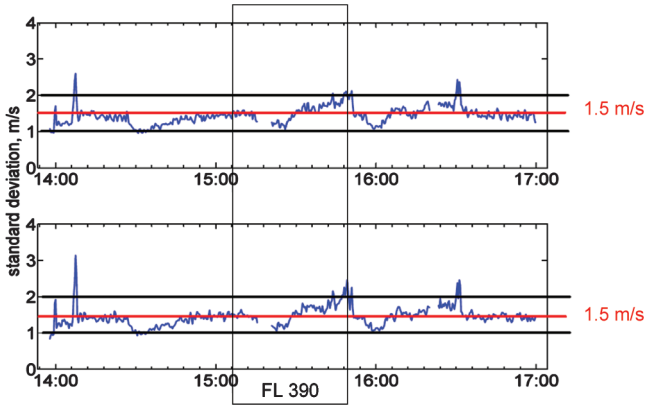

Fig. 28 Standard deviations of the vertical (lower curve) and horizontal (upper curve) components measured by the lidar sensor. FL 390 is indicated by a box.

IV. Summary of the Flight Tests

The data of the tested lidar system are compared with aircraft true-airspeed sensor data that were projected onto the LOS directions of the lidar beam directions, using aircraft attitude data, and very good correlation is found. Offsets can be compensated statically and dynamically to below 5 m/s in the lower-aerosol-concentration sequences (after aircraft takeoff) for LOS components as well as for y and z components.

It is shown that the lidar signal follows the reference aircraft-speed measurement system very well. Derived y and z components of the signal are also measured with a standard deviation of about 1.5 m/s at FL 390, to be multiplied by the geometric projection factor, depending of the measurement beam-axis angle with respect to the aircraft reference system. At the given nonoptimum 10° beam-angle setup used in these flight tests for several reasons, the factor is about 2.9. In future configurations, this angle can be increased to 35 or 45°, leading to a projection factor of 1.0 and 0.7, respectively (below 1.0 in the latter case, because of the addition of two z components at the left and the right of the aircraft body, respectively, for up and down for the y component).

A measurement range of 50 m is applied, as it was determined during the AWIATOR project to be the optimum measurement range ahead of the aircraft (which corresponds to about 74 m from the center of the measurement volume to the wing edge of the Airbus A340-300), enabling a forward-looking time of approximately 300 ms. This is sufficient for flight-control input and control-surface deflection. An overly extended measurement range would result in erroneous turbulence counteractions, due to the high dynamics of the turbulence, in which case, the aircraft would never encounter the already-moved turbulence measured at too long of a distance.

Interferograms could be recorded at all flight levels up to FL 390. At those altitudes, the aerosol backscatter signal is strongly reduced compared with ground level and is therefore much weaker than the molecular signal. This proves that the sensor is able to perform in a purely molecular environment. Sensor signals were also obtained in dense clouds in which the visibility was less than 5 m. The strong Mie scattering outweighed the effect of absorption of the laser beam by orders of magnitudes.

As has been proven in former flight tests [29], even in rain and ice rain, good sensor signals were received. Because of the gated viewing, raindrops on the window did not disturb the measurement.

V. Conclusions

A novel in-flight lidar was designed, developed, and flight-tested for the first time in a forward-looking configuration. It is based on a short-pulse UV direct-detection fringe imaging technique. It aims at measuring turbulence (even at high flight altitudes) ahead of the aircraft. Its ultimate objective is to feed forward the aircraft flight control for active counteractions.

It was shown that the direct-detection Rayleigh/Mie lidar is capable of detecting the wind speed under flight-test conditions up to cruise altitudes, in clear air, in dense clouds, in rain, and in ice rain. Standard deviations of the line-of-sight lidar signal as low as about 1.0–1.5 m/s at an altitude of 39,000 ft and measurement range of 50 m were achieved. The update rate was 60 Hz for each line-of-sight (LOS) measurement (15 Hz for full vector) and the measurement volume depth was ±15 m from center.

The sensor features clear potential for future implementation in a real-time direct-feedforward automatic-flight-control system: for example, active gust-load alleviation. A significant reduction of the turbulence loads can be achieved, as shown in the AWIATOR project, reaching the limits of the maneuver loads. A reduction of maneuver loads to an equivalent level of 2.2 g or below would allow obtaining maximum benefits of gust-load alleviation with the forward-looking lidar sensor.

This work is added to the developments and important investments that airflow remote sensing have experienced among recent years. Diverse applications would take advantage of such onboard technology as in-flight safety increase with warning systems, in-flight comfort improvement, airport capacity increase through mitigation of wake-vortex encounter issue, better-designed and more efficient aircraft, etc. The opportunity for coupling a lidar sensor to a flight controller opens a new window for improvement in the performance of aircraft. The AWIATOR sensor is designed to accomplish this ultimate objective, which is the feedforward of the wind information to the flight computers, equipped with an adequate control law. Several control strategies can be envisaged as a better distribution of the wing lift during a gust penetration. This promising application segment needs a more proven technology maturity, the capacity of the flight controllers to handle the process, and a flight-test demonstration of the benefits of the full functionality, including flights in turbulence. Therefore, in a next step, the full system capability will have to be proven in a fully integrated system test within the scope of a follow-on research and development project. It will feature the lidar sensor developed here, integrated into the skin of the aircraft, rendering a fairing unnecessary, with real-time data processing and direct feedforward to the flight-control system.

Acknowledgments

This work was supported by the European Commission under contract number G4RD-CT-2002-00836 (FP5 AWIATOR project). Many thanks to the commission and to Jens Koenig (Airbus) of AWIATOR management. The authors would like to acknowledge the effort of the whole EADS Innovation Works sensor development team [namely, Paul Zeller for development of the unique laser, Hermann Diehl and Peter Navé (Navé Applied Mathematics and Physics) for data processing algorithm development and flight-data analysis, Klaus Schertler for developing new algorithms, Guenther Reithmeier for mechanics design and integration, Stephan Stilkerich for the data recorder design and free-programmable gate array programming, Willi Platz for camera issues, and Thorstein Halldórsson for discussions on wake vortex applications] and the Airbus flight physics, flight test, and integration team (namely, Christian Lopez, Michel Lacabanne, Ludger Merz for sensor requirements, Pierre Mirand for forward-looking aircraft installation, Mael Reymond for flight-test planning, and Stephane Vaux for flight-test operation).

References

[1] "Wake Turbulence: An Obstacle to Increased Air Traffic Capacity," National Academies Press, Washington, D.C., 2008, pp. 37–40.

[2] Soreide, D., Bogue, R. K., Ehrenberger, L. J., and Bagley, H., "Coherent Lidar Turbulence Measurement for Gust Load Alleviation," NASA TM 104318, 1996.

[3] Phillips, M. W., Hannon, S. M., Henderson, S. W., Gatt, P., and Huffaker, R. M., "Solid-State Coherent Lidar Technology for Space-Based Wind Measurement," *Optics in Atmospheric Propagation, Adaptive Systems, and lidar Techniques for Remote Sensing*, Proceedings of SPIE, Vol. 2956, SPIE, Bellingham, WA, 1997,

pp. 68–75.
[4] Rothermel, J., Olivier, L., Banta, M., Hardesty, M., Howell, J., Cutten, D., Johnson, S., Menizies, R., and Tratt, D., "Remote Sensing of Multilevel Wind Fields with High-Energy Airborne Scanning Coherent Doppler Lidar," *Optics Express*, Vol. 2, No. 2, Jan. 1998, pp. 40–49. doi:10.1364/OE.2.000040
[5] Rothermel, J., Cutten, D. R., Hardesty, M., Menzies, R. T., Howell, J. N., Johnson, S. C., Tratt, D. M., Olivier, L. D., and Banta, R. M., "The Multicenter Airborne Coherent Atmospheric Wind Sensor," *Bulletin of the American Meteorological Society*, Vol. 79, No. 4, April 1998, pp. 581–599. doi:10.1175/1520-0477(1998)079<0581:TMCACA>2.0.CO;2
[6] Vaughan, J. M., Steinvall, K. O., Werner, C., and Flamant, P. H., "Coherent Laser Radar in Europe," *Proceedings of the IEEE*, Vol. 84, No. 2, Feb. 1996, pp. 205–226. doi:10.1109/5.482229
[7] Combe, H., Köpp, F., and Keane, M., "On-Board Wake Vortex Detection," *Third Wake-Net Workshop*, 22–23 May 2000, http://www.cerfacs.fr/~wakenet/instru/fields/Malvern-Article.htm [retrieved 16 Oct. 2009].
[8] Jentink, H. W., and Bogue, R. K., "Optical Air Flow Measurements for Flight Tests and Flight Testing Optical Flow Meters," National Aerospace Lab., NLR, Rept. NLR-TP-2005-256, Amsterdam, 2005.
[9] Matayosi, N., Asaka, K., and Okuno, Y., "Flight-Test Evaluation of a Helicopter Airborne Lidar," *Journal of Aircraft*, Vol. 44, No. 5, Sept.–Oct. 2007, pp. 1712–1720. doi:10.2514/1.28338
[10] Cariou, J.-P., Augere, B., Goular, D., and Schlotterbeck, J.-P., "All Fibre 1.5 μm CW Coherent Laser Anemometer DALHEC-Helicopter Flight Test Analysis," *Proceedings of the 13th Coherent Laser Radar Conference*, Tohoku Inst. of Technology, Tohoku, Japan, Oct. 2005, pp. 157–160.
[11] Woodfield, A. A., and Vaughan, J. M., "Airspeed and Wind Shear Measurements with an Airborne CO2 CW Laser," *International Journal of Aviation Safety*, Vol. 1, 1983, pp. 207–224.
[12] Morbieu, B., Combe, H., and Mandle, J., "ALEV3, a 3 AXIS CO2 CW Anemometer for Aircraft Certification," Coherent Laser Radar Conference: Applications and Technology, Universities Space Research Association, Paper MB1, 1993.
[13] Kopp, F., Werner, C., Flamant, P. H., and Loth, C., "The German-French Project WIND for the Development of an Airborne Lidar," Coherent Laser Radar Conference: Applications and Technology, Universities Space Research Association, Paper MA4, 1993.
[14] Huffaker, R. M., "Remote Sensing of Atmospheric Wind Velocities Using Solid-State and CO2 Coherent Laser System," *Proceedings of the IEEE*, Vol. 84, No. 2, Inst. of Electrical and Electronics Engineers, Piscataway, NJ, Feb 1996, pp. 181–204.
[15] Rahm, S., and Smalikho, I., "Aircraft Wake Vortex Measurement with Airborne Coherent Doppler Lidar," *Journal of Aircraft*, Vol. 45, No. 4, July–Aug. 2008, pp. 1148–1155. doi:10.2514/1.32896
[16] Soreide, D., Bogue, R. K., Ehrenberger, L. J., Hannon, S. M., and Bowdle, D, A., "Airborne Coherent Lidar for Advanced In-Flight Measurement (ACLAIM) Flight Testing of the Sensor," NASA Dryden Flight Research Center, Rept. H-2428, Edwards, CA, Sept. 2000.
[17] Hannon, S. M., Bagley, H., and Bogue, R. K., "Airborne Doppler Lidar Turbulence Detection: ACLAIM Flight Test Results," *SPIE Conference on Laser Radar Technology and Applications*, Vol. 3707, SPIE, Bellingham, WA, April 1999, pp. 234–241.
[18] "Rayleigh/Mie Lidar for Non-Intrusive Measurement of Aircraft Air Data Parameters," NASA, CR NAS4-02043, 2002, http://sbir.nasa.gov/SBIR/abstracts/01/sbir/phase1/SBIR-01-1-A7.03-8908.html [retrieved 16 Oct. 2009].
[19] Watkins, C. B., Richey, C. J., Tchoryk, P., Ritter, G. A., Dehring, M., Hays, P. M., Nardell, C. A., and Urzi, R., "Molecular Optical Air Data System (MOADS) Prototype II," *Laser Radar Technology and Applications*, Proceedings of SPIE, Vol. 5412, Bellingham, WA, 2004, pp. 10–20.
[20] Durand, Y., Meynhart, R., Endemann, M., Chinal, E., Morancais, D., Schroeder, T., and Reitebuch, O., "Manufacturing of an Airborne Demonstrator of ALADIN, the Direct-Detection Doppler Wind Lidar for ADM-Aeolus," *Lidar Technologies, Techniques and Measurements for Atmospheric Remote Sensing*, Proceedings of SPIE, Vol. 5984, Oct. 2005, Paper 598401.
[21] Schmitt, N. P., Rehm, W., Pistner, T., Zeller, P., Diehl, H., and Navé, P., "Airborne Direct-Detection UV Lidar," *Proceedings of the 23rd International Laser Radar Conference*, Conference Steering Comm., edited by C. Nagasawa and N. Sugimoto, Nara, Japan, July 2006, pp. 167–170.
[22] Jenaro, G., Mirand, P., Raymond, M., Schmitt, N. P., Pistner, T., and Rehm, W., "Airborne Forward-Looking Lidar System," International Forum on Aeroelasticity and Structural Dynamics, KTH Royal Inst. of Technology, Paper IF-088, Stockholm, 2007.
[23] Henderson, S. W., Gatt, P., Rees, D., and Huffaker, R. M., "Wind Lidar," *Laser Remote Sensing*, 1st ed., edited by T. Fujii and T. Fukuchi, Taylor & Francis, New York, 2005.
[24] Rahm, S., Smalikho, I., and Köpp, F., "Characterization of Aircraft Wake VORTICES BY Airborne Coherent Doppler Lidar," *Journal of Aircraft*, Vol. 44, No. 3, May–June 2007, pp. 799–805. doi:10.2514/1.24401
[25] Vaughan, J. M., "Scattering in the Atmosphere," *Scattering—Scattering and Inverse Scattering in Pure and Applied Science*, edited by E. R. Pike and P. C. Sabatier, Academic Press, San Diego, CA, 2002, Chaps. 2.4.3.
[26] Vaughan, J. M., *The Fabry–Perot interferometer*, 1st ed., Taylor & Francis, New York, 1989.
[27] "System and Method for the Laser Beam Deflection for Optical Measuring Systems," Rehm, W., Reithmeier, G., and Zeller, P., U.S. Patent 7,123,394 B2, 17 Oct. 2006.
[28] Hays, P. B., "Circle to Line Interferometer Optical System," *Applied Optics*, Vol. 29, No. 10, pp. 1482–1489. doi:10.1364/AO.29.001482
[29] Schmitt, N. P., Rehm, W., Pistner, T., Zeller, P., Diehl, H., and Navé, P., "The AWIATOR Airborne Lidar Turbulence Sensor," *Aerospace Science and Technology*, Vol. 11, 2007, pp. 546–552. doi:10.1016/j.ast.2007.03.006
[30] Menzies, R. T., and Tratt, D. M., "Airborne Lidar Observations of Tropospheric Aerosols During the Global Backscatter Experiment (GLOBE) Pacific Circumnavigation Missions of 1989 and 1990," *Journal of Geophysical Research*, Vol. 102, No. D3, Feb. 1997, pp. 3701–3714. doi:10.1029/96JD03405
[31] McCormick, M. P., "Simultaneous Multiple Wavelength Laser Radar Measurements of the Lower Atmosphere," *Proceedings of the Electro-Optics International 71 Conference*, Brighton, England, U.K., 24–26 March 1971, pp. 495–510.